PHYSICAL REVIEW B **97**, 094103 (2018)

Thermally induced coloration of KBr at high pressures

Sarah M. Arveson,[1,*] Boris Kiefer,[2] Jie Deng,[1] Zhenxian Liu,[3] and Kanani K. M. Lee[1]
[1]*Department of Geology and Geophysics, Yale University, New Haven, Connecticut 06511, USA*
[2]*Department of Physics, New Mexico State University, Las Cruces, New Mexico 88011, USA*
[3]*Department of Civil and Environmental Engineering, Institute of Materials Science, The George Washington University, Washington DC 20052, USA*

(Received 16 June 2017; revised manuscript received 9 January 2018; published 9 March 2018)

Laser-heated diamond-anvil cell (LHDAC) experiments reveal electronic changes in KBr at pressures between ~13–81 GPa when heated to high temperatures that cause runaway heating to temperatures in excess of ~5000 K. The drastic changes in absorption behavior of KBr are interpreted as rapid formation of high-pressure F-center defects. The defects are localized to the heated region and thus do not change the long-range crystalline order of KBr. The results have significant consequences for temperature measurements in LHDAC experiments and extend the persistence of F centers in alkali halides to at least 81 GPa.

DOI: 10.1103/PhysRevB.97.094103

I. INTRODUCTION

The existence of defects in alkali halides under irradiation is well documented [1,2]. High-intensity x-ray, UV, and infrared irradiation can generate defects that color nominally transparent alkali halides. The most prevalent color centers in KBr are F centers, which consist of an electron trapped in a Br vacancy. Models for the radiation damage process in alkali halides include formation of F centers, aggregation of defect clusters, extended defect formation, and finally annealing, when the defects decay and return to their preirradiated condition [2]. Extensive work at 300 K and below has been conducted to characterize the structure, properties, and timescales of defects during these stages. However, only a few studies have explored the effect of high temperatures or high pressures on color centers in alkali halides, and they have been limited to pressures <17 GPa [3–6]. In these studies, defects were introduced into the samples by irradiation prior to applying pressure.

We report experimental evidence for reversible defect formation in polycrystalline KBr at high pressures (13–81 GPa) and temperatures (>5000 K) using infrared laser heating that turns the initially transparent KBr opaque. KBr is an insulator with a band-gap of 7.6 eV [3], too large for direct electronic excitations from the valence band into the conduction band with infrared or visible light. However, F centers acting as electron donors cause electronic states in the band gap that affect optical properties and, in particular, absorption, and emission characteristics. Defect-related electronic changes are important for characterizing material performance, as KBr is used widely in optical devices. F centers in salts under planetary conditions may allow novel characterization of planetary and lunar surfaces [7]. Changes in absorption behavior are also crucial to temperature measurements in LHDAC experiments which often use KBr and other alkali halides as insulation media [4].

II. METHODS

A. Sample preparation

Single crystal KBr (Intl. Crystal Laboratories, 99.95% purity) was ground up into a fine polycrystalline mixture, and a 10–20-μm-thick disk was loaded into a rhenium-gasketted diamond-anvil cell with a small amount of metal foil as a laser absorber. We performed several sets of experiments using Pt, Fe, stoichiometric FeSi, or an Fe-Si9wt% alloy to ensure independence of the KBr behavior regardless of metal laser absorber. Great care was taken to prevent contamination of the samples, including drying the assemblies in an oven to minimize surface hydration. Prior to applying pressure, the LHDAC was placed in an oven at 400 K for at least 1 hour to minimize moisture in the sample chamber. We found that runaway heating and defect formation occur regardless of whether an assembly is dried under vacuum for 1 hour or 10 days. Pressure was calibrated using the high-frequency edge of the diamond Raman band [8] or the equation of state of KBr [9] for the x-ray diffraction experiments. See Table I for individual sample details.

B. Laser Heating

To generate defects in KBr, we performed high-pressure experiments in the LHDAC using a 1070 nm (~1.16 eV) fiber CW laser. The sample is subjected to either steady heating at a peak power or single-sided predefined ramp heating [10] on the KBr-side, in which the sample is annealed at a low laser power and subsequently ramped to a peak power until the laser is shut off (Table I). We positioned the laser on the edge of the metal foil during heating and collected a two-dimensional temperature map at the peak temperature using the four-color method [10]. Details on temperature measurement and accuracy can be found in Ref. [10]. To avoid damage to the diamonds, once the KBr begins absorbing the laser and thermally runs away, it remains at the peak temperature for no more than 0.3 s before the sample is temperature quenched by shutting off the laser, which takes <1 μs.

---

[*] Corresponding author: sarah.arveson@yale.edu

2469-9950/2018/97(9)/094103(10)

TABLE I. Experimental parameters for all samples in which defect formation was observed. Sample details include the alkali halide sample, metal coupler used for laser heating as well as cook time in oven at $\sim$400 K to minimize any moisture in the sample. Pressure listed is based on the high-frequency edge of the diamond Raman band [8] and is the pressure measured after heating. Uncertainties in pressure are determined by the measured pressure gradients [51]. The sample is single-sided laser heated subjected to either steady heating or predefined ramp heating [10], in which the sample is annealed at a low laser power (first power listed below) for a set amount of time (first heating duration value listed below) and subsequently ramped to a peak power (second power listed below) for one second and held constant for the remainder of the heating cycle (last time listed). For example, FeSi936s1 is annealed at a low laser power of 60 W for 2 seconds, then ramped to 90 W between 2–3 seconds and then held at 90 W from 3–4 seconds. If only one parameter is listed, ramped heating was not employed. Not all samples listed here appear in Fig. 3 due to either saturation of the charge-coupled detector (CCD), which collected the light for temperature measurement, or lack of absorption data for a temperature correction. For these saturated or uncorrected samples, the temperature listed is NA (not available). Sample names with asterisks are those with temperatures taken just as the thermal runaway was beginning and are depicted as grey diamonds in Fig. 3.

Sample name/ spot number	Sample material	Metal coupler	Pressure (GPa)	Temperature of defect formation (K)	Laser power (W)	Heating duration (s)	Cook time in oven
KBr01s2	KBr	Fe-Si9wt%	13 ± 1	NA	30	6	1 hour
KBr01s3	KBr	Fe-Si9wt%	13 ± 1	NA	30	6	1 hour
KBr02s1	KBr	Fe-Si9wt%	60 ± 2	NA	70	6	1 hour
KBr03s1	KBr	Pt	55 ± 2	NA	50	6	1 hour
KBr04s1	KBr	Fe	37 ± 2	7000 ± 700	40	6	1 hour
KBr04s2	KBr	Fe	37 ± 3	7000 ± 700	43	6	1 hour
KBr04s3	KBr	Fe	37 ± 2	7000 ± 700	45	6	1 hour
KBr05s1	KBr	FeSi	66 ± 2	7300 ± 730	90	6	3.5 hours
KBr07s1	KBr	Fe-Si9wt%	22 ± 1	5500 ± 550	60	6	1 hour
KBr07s2	KBr	Fe-Si9wt%	22 ± 1	5500 ± 550	60	6	1 hour
KBr08s2	KBr	FeSi	68 ± 2	7800 ± 100	75	6	1 hour
KBr09s1	KBr	Fe-Si9wt%	32 ± 1	NA	50	6	1 hour
KBr09s2	KBr	Fe-Si9wt%	32 ± 1	NA	50	6	1 hour
KBr10s1	KBr	Fe-Si9wt%	81 ± 2	8100 ± 100	85	6	1 hour
KBr11s1	KBr	Fe-Si9wt%	68 ± 3	NA	100	2	none
FeSi921s1*	KBr	Fe-Si9wt%	55 ± 2	4500 ± 450	50	6	1 hour
FeSi922s1	KBr	Fe-Si9wt%	54 ± 2	NA	65	6	1.5 hours
FeSi922s2	KBr	Fe-Si9wt%	54 ± 2	NA	72	6	1.5 hours
FeSi923s1	KBr	Fe-Si9wt%	53 ± 2	NA	70	2-3-4 ramped	1 hour
FeSi935s1	NaCl	Fe-Si9wt%	15 ± 1	NA	27–39 ramped	2-3-4 ramped	10 days
FeSi935s2	NaCl	Fe-Si9wt%	15 ± 1	NA	27–38 ramped	2-3-4 ramped	10 days
FeSi936s1	NaCl	Fe-Si9wt%	58 ± 2	NA	60–90 ramped	2-3-4 ramped	1 hour
FeSi938s4	CsCl	Fe-Si9wt%	50 ± 2	NA	17–45 ramped	2-3-4 ramped	1 hour
FeSi939s2	KCl	Fe-Si9wt%	45 ± 2	NA	30–50 ramped	2-3-4 ramped	1 hour
FeSi942s2	KBr	Fe-Si9wt%	13 ± 1	NA	13–26 ramped	2-3-4 ramped	1 hour
FeSi948s1	KBr	Fe-Si9wt%	22 ± 1	NA	11–22 ramped	2-3-4 ramped	1 hour
FeSi954s2	KBr	Fe-Si9wt%	32 ± 2	NA	22–46 ramped	2-3-4 ramped	1 hour
FeSi954s3	KBr	Fe-Si9wt%	32 ± 2	NA	22–45 ramped	2-3-4 ramped	1 hour
FeSi955s1*	KBr	Fe-Si9wt%	17 ± 1	3000 ± 100	15–26 ramped	2-3-4 ramped	1 hour
FeSi964s1	KBr	Fe-Si9wt%	48 ± 3	NA	21–61 ramped	2-3-4 ramped	1 hour
FeSi964s2	KBr	Fe-Si9wt%	48 ± 3	NA	21–48 ramped	2-3-4 ramped	1 hour
FeSi966s4	KBr	Fe-Si9wt%	20 ± 1	NA	10–26 ramped	2-3-4 ramped	14 hours
FeSi968s2	KBr	Fe-Si9wt%	36 ± 2	NA	17–36 ramped	2-3-4 ramped	1 hour
FeSi974s2	KBr	Fe-Si9wt%	30 ± 1	NA	20–42 ramped	2-3-4 ramped	1 hour
FeSi974s3	KBr	Fe-Si9wt%	30 ± 1	NA	20–41 ramped	2-3-4 ramped	1 hour
FeSi982s2	KBr	Fe-Si9wt%	65 ± 3	NA	32–79 ramped	2-3-4 ramped	14 hours

C. Characterization techniques

High-pressure optical absorption measurements between 450 and 1000 nm were conducted at the Infrared Lab of the National Synchrotron Light Source II at Brookhaven National Laboratory after temperature quenching. The visible absorption spectra were collected through a customized visible microscope system together with a spectrograph (SpectraPro SP-2556, Princeton Instruments) and a liquid nitrogen cooled PyLoN CCD detector. A reference spectrum was taken through an adjustable IRIS aperture at unheated and transparent KBr area at each pressure.

High-pressure synchrotron mid-IR transmission and reflection measurements were performed at beamline 1.4.3 of the Advanced Light Source, Lawrence Berkeley National Laboratory after temperature quenching. The IR spectra with 4 cm^{-1} spectral resolution were acquired through a Nicolet Magna 760 FTIR spectrometer and a custom high-pressure IR microscope system.

We collected *in situ* x-ray diffraction spectra of a 68 GPa KBr sample as defect formation occurred. Spectra were taken at Sector 16-ID-B of the Advanced Photon Source at Argonne National Lab using an x-ray wavelength of 0.4066 Å [11]. Samples were laser heated to a peak power of ~100 W and diffraction spectra were taken before, during, and after heating while at pressure and upon decompression. Raman spectra were taken with a Horiba-Jobin Yvon HR-800 Raman microscope equipped with a 50-mW green laser (532 nm) with an 1800 lines/mm grating. In order to avoid signal from the diamond anvils, spectra were taken between 100–1200 cm^{-1}.

D. Density functional theory

Three-dimensional periodic density functional theory (DFT) calculations were performed using Vienna *ab initio* simulation package (VASP) [12,13]. The electronic exchange and correlation effects were described in the GGA-PBE [14]. The interactions between atoms were described within the PAW method [15,16]. The results of this approach have been shown to be of comparable accuracy to all-electron calculations for a wide range of different materials [15]. The core region cut-off radii ($1\,\mathrm{a_B} = 0.529$ Å) of the PAW potentials were $2.8\,\mathrm{a_B}$ (core configuration $3s^2 3p^6 4s^1$) and $2.1\,\mathrm{a_B}$ (core configuration $4s^2 4p^5$), for K and Br, respectively. A plane-wave cutoff energy $E_{\mathrm{cut}} = 500\,\mathrm{eV}$ was applied throughout all calculations. F center formation energies were computed for the B1 phase at equilibrium and for the B2 phase at equilibrium (0 GPa) and 50 GPa. Following previous work [17], F centers in the B1 phase were modeled as $2 \times 2 \times 2$ supercells of the conventional unit cell (64 ions: $\mathrm{K_{32}Br_{32}}$) on a $2 \times 2 \times 2$ Γ-centered k-point grid. Similarly, F center formation energies for the B2 phase were obtained from $3 \times 3 \times 3$ supercells (54 ions, $\mathrm{K_{27}Br_{27}}$) also on a $2 \times 2 \times 2$ Γ-centered k-point grid. All structural optimizations were performed at constant pressure, and any energy contributions from zero-point motion and thermal vibrations were neglected. F centers were generated by removing one Br per supercell, and explored through spin polarized calculations were performed. Possible symmetry lowering due to F center defect formation was allowed. However, we find that during F center formation, the symmetry of the stoichiometric parent phase is preserved and local relaxation is minute. This finding is consistent with our XRD observations, which do not show any evidence for structural deviations from the defect-free B1 and B2 phases.

We use density functional theory (DFT) calculations to calculate predicted F center formation energies. As has been noted before [18], the formation of F centers is favorable in an atmosphere of excess potassium. In order to take the chemical potential(s) of the surrounding atmosphere (metal-rich) into account, we follow previous work [17]: bromine was modeled in phase I ($12 \times 12 \times 12$ Γ-centered k-point grid), which is stable at ambient pressure to at least 65 GPa [19] and potassium was modeled in its stable body-centered cubic (bcc) phase ($16 \times 16 \times 16$ Γ-centered k-point grid). F center crystals do not carry a net charge, and their formation energy can be written as in Eq. (1):

$$E_f = E_D - E_H + \mu_{\mathrm{Br}}, \tag{1}$$

TABLE II. DFT computed F center formation energies for single atom defects in KBr.

Phase	Pressure (GPa)	Br poor (F center) (eV)	K poor (eV)
B1	0	0.4	1.2
B2	0	0.5	0.5
B2	50	1.9	3.6

where E_D is the total energy (enthalpy) of the defective structure and E_H is the total energy (enthalpy) of the defect free host supercell. The chemical potential of Br is given by μ_{Br}. The conditions of thermodynamic equilibrium impose limits for the accessible range of μ_{Br}; in order for KBr to be stable against decomposition we must satisfy Eq. (2),

$$\mu_K + \mu_{\mathrm{Br}} \geqslant E_{\mathrm{KBr(s)}}, \tag{2}$$

where $E_{\mathrm{KBr(s)}}$ is the energy (enthalpy) of the defect free host phase. Thus the lower limit of μ_{Br} is given by $\mu_{\mathrm{Br}} \geqslant E_{\mathrm{KBr(s)}} - \mu_{\mathrm{K}}$ and μ_{K} is the total energy/enthalpy per atom of bcc potassium. Following the same logic, we can obtain the corresponding expression for the K-poor case. Using the total energies/enthalpies from our DFT computations, we computed defect formation energies (Table II). The results strongly suggest that the formation of an F center is endothermic but more favorable than K vacancy formation, especially at high pressures. These results advocate for F centers as the dominant defect in KBr, especially at pressures that are representative of the pressure conditions of our experiments. The energy source for F center formation is provided by the high temperatures (thermal energy) in our experiments.

The analysis of the electronic band structure shows that KBr is a wide direct-gap insulator with $E_{\mathrm{g}} = 4.3\,\mathrm{eV}$, similar to previous computations, $E_{\mathrm{g}} = 4.0\,\mathrm{eV}$ [20] and significantly lower than experiment, $E_{\mathrm{g}} = 7.4\,\mathrm{eV}$ [21] to 7.6 eV [22]. However, we note that even at the DFT level, energy differences between occupied and unoccupied states are larger than the energy of visible light. Our GW0 computational setup follows previous work [23] and improves the comparison between theory and experiment significantly, KBr in B1 phase remains a direct gap insulator with $E_{\mathrm{g}} = 7.3\,\mathrm{eV}$. In contrast, we find that KBr in B2 phase is an indirect-gap insulator with a DFT gap of $E_{\mathrm{g}} = 3.9\,\mathrm{eV}$ at equilibrium and $E_{\mathrm{g}} = 3.7\,\mathrm{eV}$ at 50 GPa. The GW0 increases E_{g} to 6.6 eV and 6.2 eV at equilibrium and 50 GPa, respectively, and confirms that the B2 phase is an indirect gap insulator. Thus KBr is expected to be optically transparent for visible light in both the B1 and the B2 phases, as observed experimentally.

F centers create paramagnetic centers with defect levels deep within the fundamental gap of the host crystal [17]. The same work for NaCl in the B1 phase shows that hybrid functionals increase the band gap and shift the defect level deeper into the band-gap (relative to the conduction band minimum). We find qualitatively similar behavior in KBr: the F center separation from the conduction band minimum is 0.8, 0.7, and 1.0 eV for B1 at equilibrium, B2 at equilibrium, and B2 at 50 GPa, respectively. Our PBE0 computations show similar pressure dependence (the amount of exact exchange was adjusted such that the PBE0 [24] computations matched

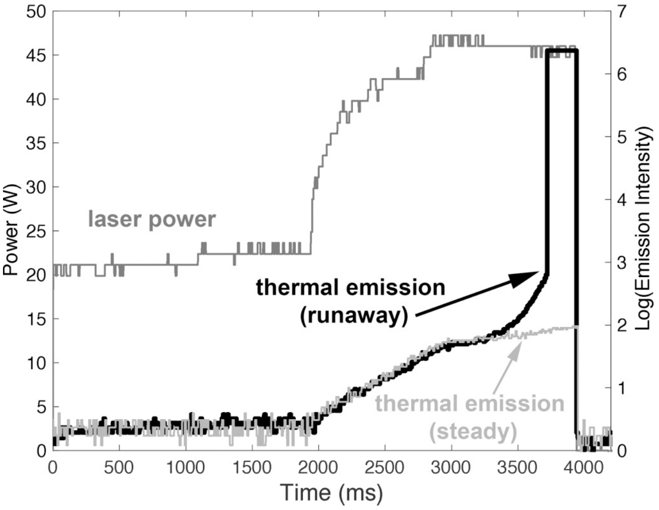

FIG. 1. A representative evolution of laser power (dark grey curve), thermal emission while heating vs time for a sample without defect formation (light grey thin curve), and thermal emission while heating vs time for a saturated defect formation sample, e.g., FeSi954s2 (black thick curve). For the defect-saturated sample, runaway heating begins at ~3700 ms, and goes from relatively steady heating to runaway in <1 ms (the time resolution of the photodiode). For the defect-free sample, emission plateaus at the peak power.

the $GW0$ computed electronic structure: 38.7%, 36.0%, and 33.0% for B1 at equilibrium, B2 at equilibrium, and B2 at 50 GPa, respectively). The respective F center induced defect states with these parameters are located 2.6, 2.3, and 3.2 eV below the conduction band minimum. However, the exact location of the defect level and the inferred optical properties from DFT and post-DFT computations must be considered uncertain even at equilibrium [17].

III. RESULTS AND DISCUSSION

A. Onset of defect formation

Below a critical temperature, KBr insulates the metal and is transparent to the infrared laser as in previous studies. At or above the critical temperature, near the projected melting temperature of KBr [25], the KBr absorbed the laser radiation directly, leading to runaway temperatures in excess of 5500 K. Once runaway absorption from the KBr began, the laser was shut off to allow rapid (<1 μs) temperature quenching [26] (Fig. 1).

Upon temperature quenching, we found that the heated KBr had become opaque to visible light when heated above 20 GPa [Figs. 2(a) and 2(b)]. Between 13 and 20 GPa, the heated KBr turned a semitransparent orange color. Owing to efficient thermal conductivity of diamond, temperature gradients in the LHDAC are necessarily large [27]. The absorption decreases radially outward from the laser focal spot, indicating strong temperature dependence, consistent with experiments at ambient pressure that showed higher F center concentrations with increasing temperatures [28]. The resulting thickness of the defect-damaged KBr was 1–2 micrometers, determined by interference fringes in infrared reflectivity measurements. The temperature required to initiate coloration in KBr increases with increasing pressure (Fig. 3). The increase in temperature required for defect formation with pressure can be attributed to a greater amount of thermal energy required to liberate atoms from their equilibrium positions at higher density. Because there is a short (order 10 picoseconds) but finite time range

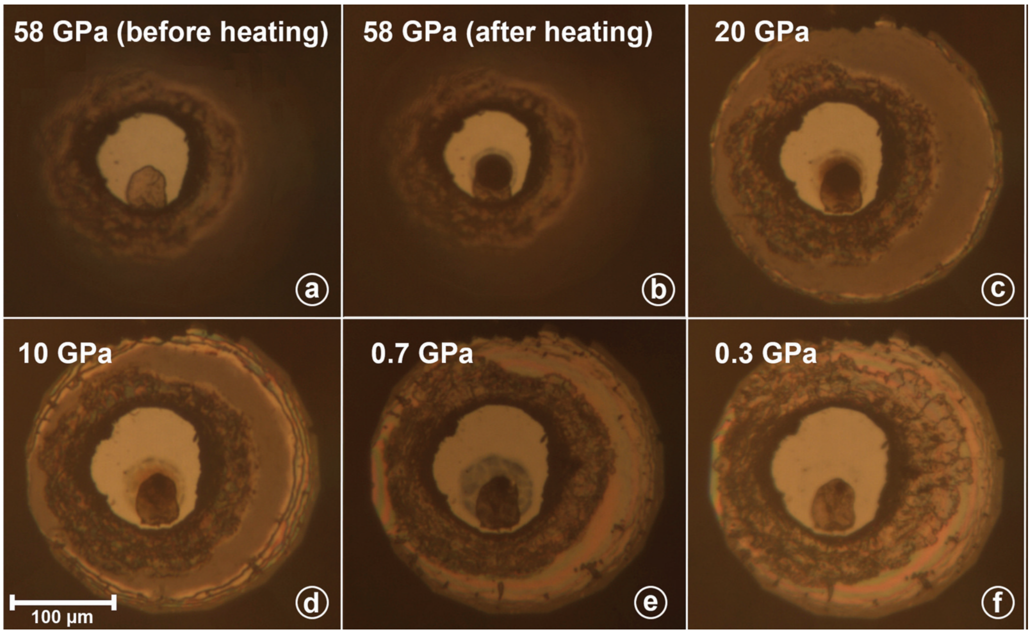

FIG. 2. Optical images of defect-damaged KBr02s1 during decompression. Images were taken while at pressure in a LHDAC using both reflected and transmitted light. (a) Before heating, only the metal foil, used as a laser absorber, is visible in the gasket hole, surrounded by transparent KBr. (b) When heated on the tip of the metal foil, the KBr becomes absorbing, and the entire heated region of KBr darkens. (c)–(f) Upon decompression, the defect-damaged KBr becomes less absorbing, progressing from black to orange, to blue after the B2 to B1 phase transition at ~1.8 GPa, and eventually returning to transparent at room pressure.

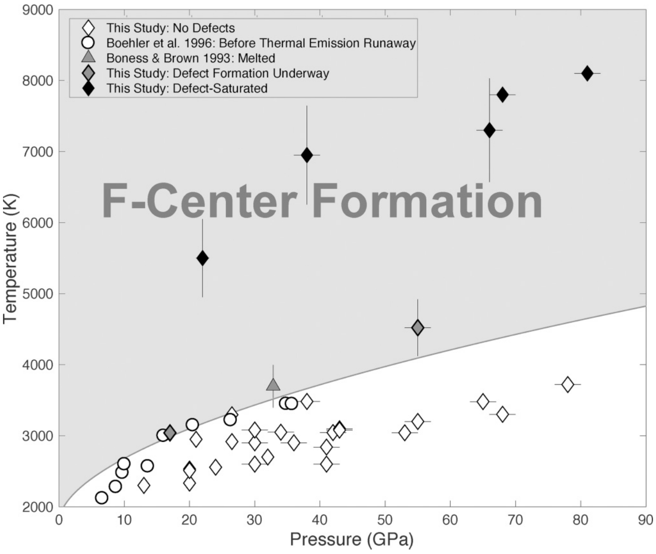

FIG. 3. Estimated temperatures required for the onset of rapid F center formation in KBr at high pressures. At the curve, runaway heating begins, and above the curve, F centers are present in KBr. Diamond symbols are temperature measurements from this study. Error bars for open diamonds are of the same size or smaller than the symbols ($\leqslant \pm 100$ K). Circles [25] represent the last temperature measured before thermal runaway. The grey triangle [32] from a shock study pins down the melting temperature of KBr. Open symbols represent measurements of KBr in which no defects were observed, and filled symbols represent defect formation underway (grey symbols) and defect-saturated (black symbols) samples. The curve is speculative and fit using previous data [25] as a tight lower bound to onset of defect formation up to ∼36 GPa together with our measurements at 17 and 55 GPa as upper bounds to the onset of defect formation.

between onset of defect formation [29], F centers develop in KBr before thermal runaway is complete. Two data points (Fig. 3 filled grey diamonds) demonstrate the case that defect formation began but did not reach the saturation limit. This is evidenced by a smaller change of opacity than samples of the same pressure that underwent complete thermal runaway and a thermal emission profile that did not saturate.

B. Pressure-dependent absorption

While no *in situ* absorption measurements were made at high temperature due to technical unfeasibility, fast laser shutoff rates ($\sim 1\ \mu$s) and a rapid change in thermal emission in <1 ms strongly suggest that the coloration observed after temperature quenching is inherited from defects formed at high temperatures. Absorption measurements were taken in the visible and infrared wavelengths after temperature quenching while the samples were still at pressure. Absorbance is found to increase with increasing synthesis pressure (Fig. 4), approaching a grey body by 81 GPa.

The lack of absorption edges rules out the possibility of an insulator to metal transition occurring in the KBr. A shift and broadening of the F absorption band is in accordance with the Mollwo-Ivey relationship that predicts the peak position of the F band depends primarily on the lattice constant of the host crystal [6,30,31]. The pressure effect can be qualitatively explained by a decreasing energy difference between the electronic F center level and conduction band with pressure, consistent with a pressure induced broadening of the conduction band.

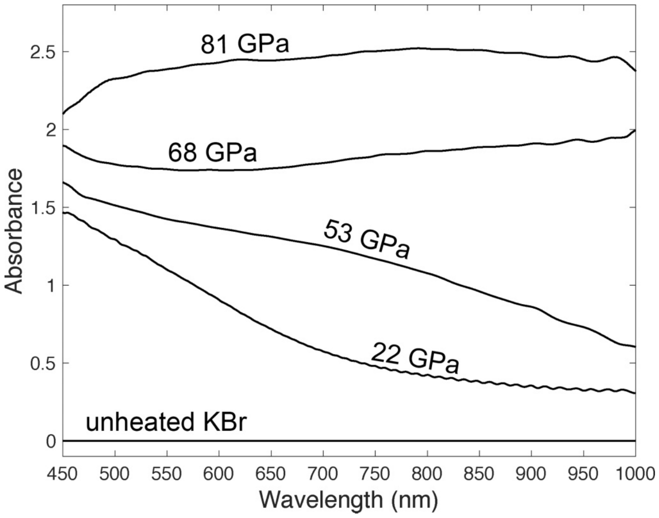

FIG. 4. High-pressure visible absorbance spectra for defect-damaged KBr samples (KBr07s1, FeSi923s1, KBr08s2, KBr10s1) after quenching from high temperature. The thickness of the defect-damaged region is 1 μm. Unheated and un-defected KBr, regardless of the pressure, remains transparent in the wavelength range considered.

C. Crystal structure and the melting curve of KBr

This rapid change in absorption and emission during laser heating has been previously observed and attributed to the melting of KBr [25]. Given that the optical change was the sole criterion to identify the melting point in that study, our observations suggest that melting is not a prerequisite for thermal runaway—either defect formation occurs before melting or melting and defect formation begin concurrently. Therefore the only current definitive point on the high-pressure KBr melting curve is given by shock compression experiments [32] that reveal melting along the Hugoniot at 33 GPa.

Transparent KBr is expected to remain in the B2 cubic phase in the pressure range we consider [9] and is expected to be molten at the runaway temperatures ($\sim 5000 +$ K) we measure on the absorbing KBr according to the existing high-pressure melting curve [25]. The structure of defect-damaged KBr has not been characterized at these high pressures or high temperatures. In addition, tetragonal and orthorhombic phases have been predicted for KCl, another potassium halide, at extreme conditions exceeding 200 GPa [33]. Our *in situ* x-ray diffraction (XRD) measurements on KBr show no evidence of phase transitions or any other unexplained diffraction peaks, indicating that the KBr remained in the B2 phase or a new phase was produced in too small amounts to be detected by XRD (Fig. 5). Diffraction patterns rule out the possibility of chemical reactions between the KBr and the metal absorber, or dissociation of KBr as observed with CsI at high pressure and high temperature [34]. No diffuse melt signal was observed, suggesting that the KBr became absorbing in the solid state,

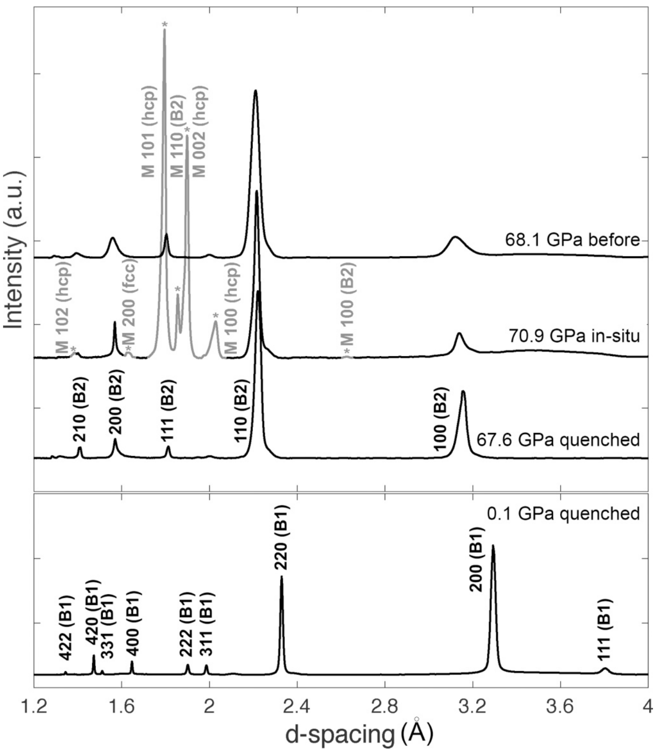

FIG. 5. (Top) XRD pattern taken at 68.1 (±0.1) GPa before heating, 70.9 (±0.1) GPa during runaway heating to ∼8000 K, and after heating at 67.6(±0.1) GPa on the darkened defect-damaged sample KBr11s1. Grey peaks with asterisks and labeled M correspond to hcp, B2, and fcc Fe-Si9wt% solid phases of the metal coupler. KBr remains structurally closed with respect to the B2 phase during defect formation. Despite the high temperatures while in thermal runaway, the FeSi9wt% metal coupler remains in its solid state. (Bottom) XRD pattern of KBr quenched to near room pressure that has reverted back to the B1 phase. See also Fig. S1 in Ref. [44] for raw data.

or potentially as a premelting effect as previously suggested [35]. In KCl, for instance, the F center concentration increases rapidly just below the melting temperature [29]. However, the strong recrystallization texture of B2 KBr after quenching temperature suggests that KBr did melt after thermal runaway in regions that became opaque, but likely only in a small and localized region (Fig. S1 in Ref. [44]). To bound the temperature difference between when defect formation occurs and when melting occurs would require a technique with simultaneous ultrafast temperature measurement and ultrafast structural characterization.

D. Activation of Raman modes

While XRD captures the long-range order that remains virtually unaffected, Raman spectroscopy reveals symmetry breaking in the local structure. Our defect-damaged KBr exhibits strong Raman-active modes at high frequencies (Fig. 6). The Raman peaks become more intense and shift to lower frequencies as the sample is decompressed in the B2 phase. Vibrational frequencies increase during the phase transition below 2 GPa in accordance with the elastic response of the B2 to B1 transition [36]. At ambient pressure, the Raman signal is lost and cannot be recovered upon recompression. Given that Raman spectra are robust among samples heated with different metal couplers Fe, FeSi, Fe-Si9wt%, and Pt (Fig. S2 in Ref. [44]), we infer that this is an intrinsic KBr defect rather than due to diffusion of metal impurities into the KBr, which can also break translational invariance of the lattice and induce first order Raman modes [37]. For any given pressure, the Raman spectra were identical regardless of the metal used. Examples of defect-damaged KBr using Pt or FeSi9wt% are shown in Fig. S2 in Ref. [44] for ∼56 GPa and on decompression to ∼4.5 GPa. The similarity in spectra, especially on decompression when hysteresis effects can be large, provides compelling evidence that the defect is intrinsic to KBr. This is reinforced by the observation that no new phases appear in the in-situ diffraction spectra (Fig. 5). Indeed, a quick comparison between our Raman spectra and that of impurity-induced Raman spectra of KBr [37] show little similarities, in large part due to the broad peaks and the small frequencies (most $<100\ \mathrm{cm}^{-1}$) they measure and our inability to measure frequencies less than $100\ \mathrm{cm}^{-1}$.

E. Stability of F centers

Upon decompression to room pressure, KBr reverts to the B1 structure with no memory of damage (Fig. 5). The color centers in KBr are annealed during decompression, which is apparent throughout the Raman spectra (Fig. 6), optical images [Fig. 2(e)], and absorbance spectra (Fig. S3 in Ref. [44]). The KBr becomes progressively less opaque, evolving from black above 20 GPa to a bright blue color below ∼2 GPa (Fig. 2), consistent with the color centers observed in lower pressure studies of KBr [38,39]. For this reason, we attribute this defect state to high-pressure F centers in KBr. This is in contrast with early work that observed an increase in absorption energy of the F center in KBr with pressures to ∼15 GPa and predicted a continual increase in the absence of a phase transition [3,4]. These studies generated F centers at room pressure and temperature conditions using x irradiation, and defected samples were subsequently taken to pressures much lower than those achieved in our study. The thermal energies of these LHDAC experiments exceed 0.43 eV (nominal $T = 5000$ K). This is comparable to the energy range used in recent short-lived F center studies using other defect-forming techniques [1,2,40,41]. The absence of an XRD signal from the defects and the presence of Raman peaks indicate that the defects are localized to the heated region. In our DFT calculations, we relax KBr F centers in the B1 and B2 phases and confirm that structural distortions are very small, consistent with previous work [17]. Furthermore, symmetry analysis of the computationally relaxed structures shows that the resulting structures can be described within the same space group as B2, consistent with our XRD observations. The number of Raman modes observed in our study is consistent with previous observations in the B1 KBr phase that have been attributed to F centers [37]. Previous work finds that optical F-band absorption energy, attributed to the $1s$-to-$2p$ transition [42], increases with decreasing volume (increasing pressure) [6]. With increasing pressure, the conduction bandwidth and F-center transition energies increase which suggests that during relaxation after the optical excitation, a larger amount of energy

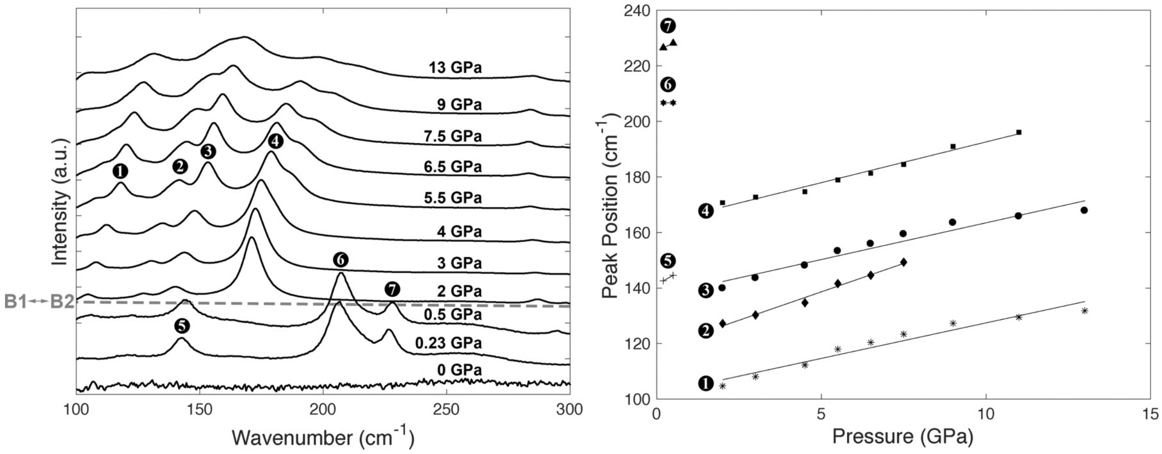

FIG. 6. (Left) Raman spectra of defect-damaged sample KBr01s3 synthesized at 13 GPa on decompression. Horizontal dashed line corresponds to the B1 → B2 phase boundary, which occurs at pressures <2 GPa. (Right) Evolution of peak frequencies with pressure during decompression.

can be converted to phonons, consistent with the runaway heating observed experimentally.

While F centers in KBr have shown to be stable in the range of microseconds [40,43] to a year [39], we have observed the stability of the defects through sustained coloration for greater than 1 month prior to decompression. If left under pressure, lifetimes may be much longer. A recent study that observed comparatively long stability timescales of one year for color centers in KBr required femtosecond laser pulse energies of 31–156 GeV [39] and observed increasing defect density with increasing energy, in concordance with our observations. At 68 GPa, a combined pressure-volume and thermal energy of ~30 eV was sufficient to stabilize defects for a minimum of one month [44]. The Raman vibrational spectra suggest a strong pressure dependence of the stability and optical properties of F centers and leave the aspect of time as an open area of future research.

IV. APPLICATION TO TEMPERATURE CORRECTION

Accurate temperature measurements at high pressure have been a difficult task throughout the history of laser heating [45]. While progress has been made in careful temperature measurements, the contribution of wavelength-dependent absorption has only recently been considered [46]. KBr and other salts are frequently used as insulation in LHDAC experiments under the assumption that they remain transparent in the visible wavelength range. Noble gases are used as insulation for similar reasons, but they also become opaque at high pressures and temperatures [47]. Most laser heating is performed in a hutch at a synchrotron, so temporal evolution of heating is difficult to monitor. Additionally, heating is typically performed with KBr overlying opaque materials so that a change in KBr color is not distinguishable from sample color or changes in sample color. For these reasons, the absorbing behavior in salts at extreme conditions is not well documented despite potential issues in LHDAC experiments. Wavelength-dependent absorption (Fig. 4) due to defects may cause temperature deviations of hundreds to thousands of degrees, resulting in incorrectly interpreted temperatures [46] (Figs. 7 and 8).

We measure temperature using four-color multiwavelength imaging radiometry [10]. Intensity of light from the sample is measured at four wavelengths: 580, 640, 766, and 905 nm in the area of the hotspot, and we use a Wien fit to obtain a two-dimensional map of the apparent temperature (T_a) as shown in Fig. 7. In the case of a transparent insulation medium overlying a blackbody laser absorber, the apparent temperature is nearly equal to the real temperature (T_r). In the case that either the insulation medium or the laser absorber has variable wavelength-dependent absorption, $T_a \neq T_r$, and a temperature correction is required [46], as shown for four specific samples

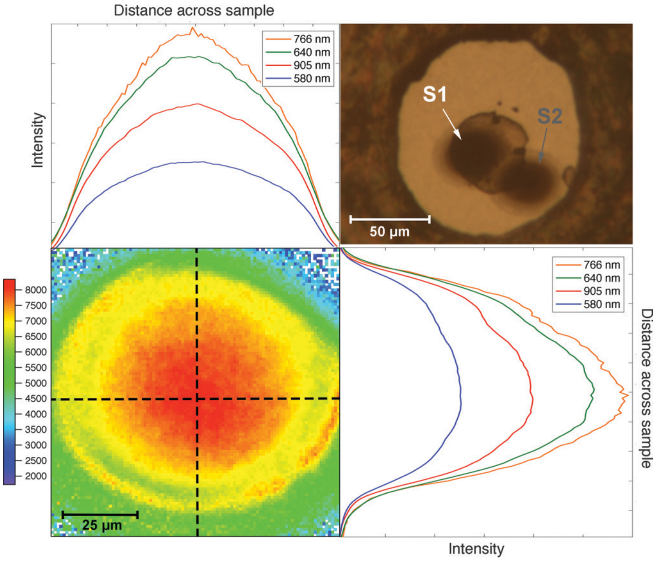

FIG. 7. Uncorrected 2D temperature map for a defect-damaged sample KBr07s1 at 22 GPa. (Upper left and lower right) Horizontal and vertical intensity profiles along the dashed transects marked on the temperature map. (Upper right) Optical image showing two heated and defect-damaged spots using both reflected and transmitted light.

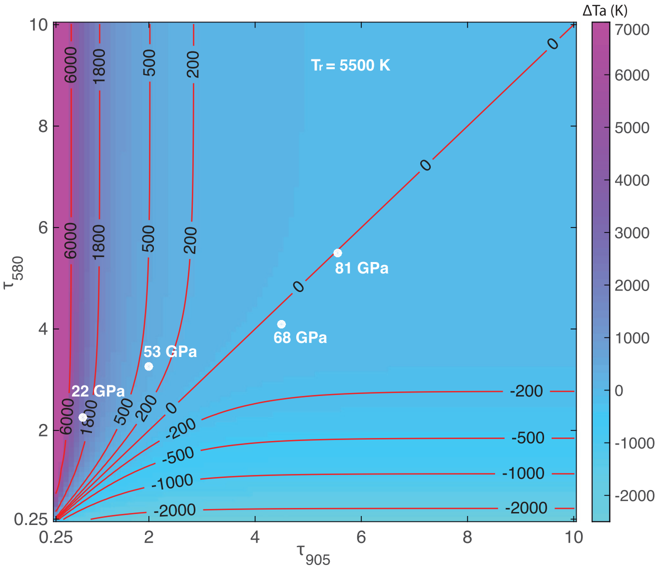

FIG. 8. Effect of wavelength-dependent absorption from defect-damaged KBr on temperature measurements at a nominal maximum real temperature of 5500 K (see Ref. [46] for more details). The axes represent optical thickness at 580 nm and 905 nm, respectively, for an absorbing hotspot 1 μm in thickness. The color gradient and corresponding contours show the deviation of apparent measured temperature from the real temperature ($T_a - T_r$). Thus, for Fig. 7, the sample at 22 GPa has a measured peak temperature in excess of 8000 K. However, due to the strong wavelength-dependent absorbing nature of a sample heated at those pressures, the real temperatures is ∼5500 K, which is 2600 K lower than what was measured.

of color center-defected KBr in Fig. 8. Figure 7 shows a hotspot measured while KBr began to absorb the laser. While the laser is ramped to a peak power and held steady, the thermal emission begins to rapidly increase once defect formation begins (Fig. 1). Lineout intensity profiles measured at four different wavelengths reveal intensities that decrease radially outward so that temperature should also decrease radially outward. Upon inspection of the temperature map, this does not hold throughout the hotspot when fit to a uniform blackbody spectrum. At 22 GPa, the absorption profile in the center of the hotspot absorbs more at shorter wavelengths (Fig. 4), causing a higher apparent temperature than the sample truly experiences. Moving outward from the center of the hotspot in Fig. 7, large temperature gradients correspond to drastic changes in defect concentration, or opacity. The wavelength-dependent absorption profile changes significantly moving outward from the hotspot, leading to apparent higher temperatures at the edge of the hotspot, which is unphysical and inconsistent with the monotonically decreasing intensities.

Even with the temperature correction shown, it is noted that T_r is representative of the temperature of the KBr and not the temperature of the laser absorber. Once the KBr forms an absorbing layer, the metal becomes poorly insulated. To obtain the temperature of the laser absorber in order to correct previous melting curves, for instance, the KBr cannot be opaque. If the KBr is semitransparent, then extensive thermal modeling based on sample geometry is required to determine the temperature of the laser absorber and is left for future work. Else, if the KBr becomes opaque, the temperature measured will be approximately the temperature of KBr with minimal temperature correction. Figure 8 shows the deviation of apparent temperature (T_a) from real temperature (T_r) in optical thickness space, with T_r being the maximum temperature reached by the 22 GPa sample in Fig. 4. The optical thickness τ_λ is given by $\tau_\lambda = \int_0^d k_\lambda dz$, where k_λ is the absorption coefficient at wavelength λ and d is the thickness of the material that participates in radiative heat transfer at wavelength λ. For this scenario, d is the thickness of the resulting defect-damaged KBr. At 22 GPa, the correction is drastic. The temperature map collected prior to any temperature correction due to wavelength-dependent absorption (Fig. 4), yields a peak temperature of ∼8100 K (Fig. 7), which is ∼2600 K greater than the real temperature of 5500 K (Fig. 8). When defects are generated at higher pressures such as at 81 GPa, the grey body assumption becomes valid once more (Fig. 4), so that the measured temperature of the defected KBr itself is valid, noting that it is the defected KBr temperature that is being measured rather than the underlying sample. Characterizing high-pressure, high-temperature defect properties may offer an explanation for highly contested data sets such as the high-pressure melting curve of iron. The experimental melting curve of iron, though studied for decades, still shows discrepancies of ∼1000 K when extrapolated to Earth's innercore boundary pressure of ∼330 GPa [48–50]. Defect-related optical changes in the alkali halides used to insulate the iron may provide an explanation for these observed large discrepancies and directly affect our understanding of the evolution of earth.

V. CONCLUSIONS

We observe a wide range of thermally-induced coloration in KBr in the LHDAC based on synthesis pressure. While *in situ* XRD reveals no significant change in bulk structure, emergence of strong Raman modes and wavelength-dependent absorption in the initially transparent KBr indicate the generation of F centers at high pressure and temperature. When held at pressure, annealing of defects is stalled compared to room-pressure studies, with coloration persisting for at least one month. Since diamonds are opaque to UV radiation and defects are annealed on decompression, the ability to probe excitonic features in the LHDAC is limited. Otherwise, photoluminescence spectroscopy and UV absorption would aid in confirming this phenomenon and determining the electronic signature of the defect state. While it is not possible to determine if KBr melting occurs just prior to, concurrent with, or just after thermal runaway with our measurements, it is possible to conclude the simultaneity of defect formation with thermal runaway. While the observation of thermal runaway was previously used to infer onset of melting of KBr at high pressures [25], this study concludes that defect formation is the physical cause of observed thermal runaway but is still a good indicator of melting within high-pressure temperature measurement errors. If amorphous melt diffraction can be identified while monitoring finely time-resolved thermal emission, this would provide a diagnostic to determine whether the defect formation occurs before, during, or after melting of KBr.

While we direct our attention to the coloration of KBr at high pressures and temperatures, we note that the runaway temperature effect due to defect formation is likely a robust phenomenon for all alkali halides. In a few separate experiments (Table I), we observed similar color changes in NaCl, KCl, and CsCl at high pressures. Because of the ubiquitous use of KBr and other alkali halides in LHDAC experiments as insulation and/or as a pressure medium/calibration standard [51], its coloration at high pressures and temperatures is of special concern to our understanding of high-energy density physics.

ACKNOWLEDGMENTS

This work was funded by an NSF CAREER grant to K.K.M.L. (EAR-0955824) and a NASA CT Space Grant to S.M.A. (PTE Federal Award No: NNX15AI12H) XRD experiments were performed at HPCAT (16-ID-B), Advanced Photon Source (APS), Argonne National Laboratory. HPCAT operations are supported by DOE-NNSA under Award No. DE-NA0001974, with partial instrumentation funding by NSF. The Advanced Photon Source is a U.S. Department of Energy (DOE) Office of Science User Facility operated for the DOE Office of Science by Argonne National Laboratory under Contract No. DE-AC02-06CH11357. Absorption measurements were made at the Infrared Laboratory at the National Synchrotron Light Source II (NSLS-II). The Infrared Laboratory is supported by COMPRES, the Consortium for Materials Properties Research in Earth Sciences under NSF Cooperative Agreement EAR 1606856 and the DOE/National Nuclear Security Administration under Grant DE-NA-0002006, Carnegie DOE Alliance Center (CDAC). NSLS-II is supported by the DOE Office of Science under Contract No. DE-SC0012704. High-pressure synchrotron mid-IR transmission and reflection measurements were performed at beamline 1.4.3 of the Advanced Light Source, Lawrence Berkeley National Laboratory. The Advanced Light Source, which is a DOE Office of Science User Facility under contract No. DE-AC02-05CH11231. Computing resources were provided through the National Science Foundation (XSEDE) under Grant No. DMR TG-110093.

[1] F. Seitz, Rev. Mod. Phys. **18**, 384 (1946).
[2] C. R. A. Catlow, K. M. Diller, and L. W. Hobbs, Philos Mag A **42**, 123 (1980).
[3] W. G. Maisch and H. G. Drickamer, J. Phys. Chem. Solids **5**, 328 (1958).
[4] R. A. Eppler and H. G. Drickamer, J. Chem. Phys. **32**, 1418 (1960).
[5] I. S. Jacobs, Phys. Rev. **93**, 993 (1954).
[6] C. J. Buchenauer and D. B. Fitchen, Phys. Rev. **167**, 846 (1968).
[7] M. J. Poston, R. W. Carlson, and K. P. Hand, J. Geophys. Res.: Planets **122**, 2644 (2017).
[8] Y. Akahama and H. Kawamura, J. Appl. Phys. **96**, 3748 (2004).
[9] A. Dewaele, A. B. Belonoshko, G. Garbarino, F. Occelli, P. Bouvier, M. Hanfland, and M. Mezouar, Phys. Rev. B **85**, 214105 (2012).
[10] Z. X. Du, G. Amulele, L. R. Benedetti, and K. K. M. Lee, Rev. Sci. Instrum. **84**, 075111 (2013).
[11] Y. Meng, G. Shen, and H. K. Mao, J. Phys-Condens Mat. **18**, S1097 (2006).
[12] G. Kresse and J. Furthmuller, Comp. Mater. Sci. **6**, 15 (1996).
[13] G. Kresse and J. Furthmuller, Phys. Rev. B **54**, 11169 (1996).
[14] J. P. Perdew, K. Burke, and M. Ernzerhof, Phys. Rev. Lett. **77**, 3865 (1996).
[15] G. Kresse and D. Joubert, Phys. Rev. B **59**, 1758 (1999).
[16] P. E. Blochl, Phys. Rev. B **50**, 17953 (1994).
[17] W. Chen, C. Tegenkamp, H. Pfnür, and T. Bredow, Phys. Rev. B **82**, 104106 (2010).
[18] F. Seitz, Rev. Mod. Phys. **26**, 7 (1954).
[19] A. San-Miguel, H. Libotte, M. Gauthier, G. Aquilanti, S. Pascarelli, and J.-P. Gaspard, Phys. Rev. Lett. **99**, 015501 (2007).
[20] P. K. de Boer and R. A. de Groot, Eur. Phys. J. B **4**, 25 (1998).
[21] F. C. Brown, C. Gahwiller, H. Fujita, A. B. Kunz, W. Scheifley, and N. Carrera, Phys. Rev. B-Solid St. **2**, 2126 (1970).
[22] D. Grojo, S. Leyder, P. Delaporte, W. Marine, M. Sentis, and O. Uteza, Phys. Rev. B **88**, 195135 (2013).
[23] M. Shishkin and G. Kresse, Phys. Rev. B **75**, 235102 (2007).
[24] C. Adamo and V. Barone, J. Chem. Phys. **110**, 6158 (1999).
[25] R. Boehler, M. Ross, and D. B. Boercker, Phys. Rev. B **53**, 556 (1996).
[26] Z. Du, J. Deng, and K. K. M. Lee, Geophys. Res. Lett. **44**, 12190 (2017).
[27] W. Panero and R. Jeanloz, J. Geophys. Res. **106**, 6493 (2001).
[28] J. D. Comins, Phys. Status Solidi B **43**, 101 (1971).
[29] R. T. Williams, J. N. Bradford, and W. L. Faust, Phys. Rev. B **18**, 7038 (1978).
[30] H. F. Ivey, Phys. Rev. **72**, 341 (1947).
[31] P. Tiwald, F. Karsai, R. Laskowski, S. Gräfe, P. Blaha, J. Burgdörfer, and L. Wirtz, Phys. Rev. B **92**, 144107 (2015).
[32] D. A. Boness and J. M. Brown, Phys. Rev. Lett. **71**, 2931 (1993).
[33] A. Shamp, P. Saitta, and E. Zurek, Phys. Chem. Chem. Phys. **17**, 12265 (2015).
[34] Q. Williams and R. Jeanloz, Phys. Rev. Lett. **59**, 1132 (1987).
[35] J. L. Tallon, W. H. Robinson, and S. I. Smedley, J. Phys. Chem. **82**, 1277 (1978).
[36] A. M. Hofmeister, Phys. Rev. B **56**, 5835 (1997).
[37] B. N. Ganguly and M. Nicol, J. Appl. Phys. **47**, 2467 (1976).
[38] H. Sothe, J. M. Spaeth, and F. Luty, J. Phys-Condens. Mat. **5**, 1957 (1993).
[39] X. W. Wang, R. Buividas, F. Funabiki, P. R. Stoddart, H. Hosono, and S. Juodkazis, Appl. Phys. A **122**, 194 (2016).
[40] J. T. Dickinson, S. C. Langford, S. M. Avanesyan, and S. Orlando, Appl. Surf. Sci. **253**, 7874 (2007).
[41] D. W. Lynch and D. A. Robinson, Phys. Rev. **174**, 1050 (1968).
[42] J. H. Simpson, Proc. R. Soc. Lon. Ser.-A **197**, 269 (1949).
[43] R. K. Swank and F. C. Brown, Phys. Rev. **130**, 34 (1963).
[44] See Supplemental Material at http://link.aps.org/supplemental/10.1103/PhysRevB.97.094103 for experimental details and suppemental figures.
[45] R. Jeanloz and A. Kavner, Philos T R Soc. A **354**, 1279 (1996).

[46] J. Deng, Z. Du, L. R. Benedetti, and K. K. M. Lee, J. Appl. Phys. **121**, 025901 (2017).

[47] R. S. McWilliams, D. A. Dalton, Z. Konopkova, M. F. Mahmood, and A. F. Goncharov, P. Natl. Acad. Sci. USA **112**, 7925 (2015).

[48] R. Boehler, D. Santamaria-Pérez, D. Errandonea, and M. Mezouar, J. Phys. Conf. Ser. **121**, 022018 (2008).

[49] S. Anzellini, A. Dewaele, M. Mezouar, P. Loubeyre, and G. Morard, Science **340**, 464 (2013).

[50] J. M. Jackson, W. Sturhahn, M. Lerche, J. Zhao, T. S. Toellner, E. E. Alp, S. V. Sinogeikin, J. D. Bass, C. A. Murphy, and J. K. Wicks, Earth Planet Sc. Lett. **362**, 143 (2013).

[51] I. Uts, K. Glazyrin, and K. K. M. Lee, Rev. Sci. Instrum. **84**, 103904 (2013).